

Experiments and numerical simulation of wire and arc additive manufactured steel materials

Xin, Haohui; Tarus, Iulia; Cheng, Lu; Veljkovic, Milan; Persem, Nicolas; Lorch, Laurent

DOI

[10.1016/j.istruc.2021.08.055](https://doi.org/10.1016/j.istruc.2021.08.055)

Publication date

2021

Document Version

Final published version

Published in

Structures

Citation (APA)

Xin, H., Tarus, I., Cheng, L., Veljkovic, M., Persem, N., & Lorch, L. (2021). Experiments and numerical simulation of wire and arc additive manufactured steel materials. *Structures*, 34, 1393-1402. <https://doi.org/10.1016/j.istruc.2021.08.055>

Important note

To cite this publication, please use the final published version (if applicable). Please check the document version above.

Copyright

Other than for strictly personal use, it is not permitted to download, forward or distribute the text or part of it, without the consent of the author(s) and/or copyright holder(s), unless the work is under an open content license such as Creative Commons.

Takedown policy

Please contact us and provide details if you believe this document breaches copyrights. We will remove access to the work immediately and investigate your claim.

Green Open Access added to TU Delft Institutional Repository

'You share, we take care!' - Taverne project

<https://www.openaccess.nl/en/you-share-we-take-care>

Otherwise as indicated in the copyright section: the publisher is the copyright holder of this work and the author uses the Dutch legislation to make this work public.



Experiments and numerical simulation of wire and arc additive manufactured steel materials

Haohui Xin^{a,b,*}, Iulia Tarus^b, Lu Cheng^b, Milan Veljkovic^b, Nicolas Persem^c, Laurent Lorich^c

^a Department of Civil Engineering, Xi'an Jiaotong University, Xi'an, China¹

^b Civil Engineering and Geosciences, Delft University and Technology, Netherland²

^c ArcelorMittal Global R&D Bars & Wires, France

ARTICLE INFO

Keywords:

Wire arc additive manufacturing
Finite element simulation
Material tests

ABSTRACT

In recent years, wire arc additive manufacturing (WAAM) has increasingly attracted attention in the construction sector because of its ability to optimize the production of large metallic structural parts, and for use in connections suitable for easy execution and potential reuse. The technology has become mature leading to shorter fabrication times and less expensive total costs due to lower raw material costs. Therefore, it is timely to conduct the material tests to evaluate the plastic flow and fracture of the WAAM steel plate to gain material characterization for an efficient design of connections. In this paper, the coupon specimens are cut from the WAAM plates in different directions in relation to the printing orientation to investigate possible material anisotropy. Results of uniaxial coupon specimens, the stress-strain curve, are analyzed in three stages: the elastic stage, the plastic stage and the coupled plastic-damage stage. The FE simulation is performed to calibrate the true stress and strain curves in different stages.

1. Introduction

Additive manufacturing (AM), also referred to as 3D printing, is a technology that forms three-dimensional objects by placing successive layers of raw materials. AM is becoming popular in the construction sector [1–5] attributing to its rapid prototyping advantages. Seven types of distinct processes of AM processes are recognized by ISO/ASTM 52,900 [6] as follows: material extrusion, material jetting, binder jetting, powder bed fusion, directed energy deposition, vat photopolymerization, and sheet lamination. In recent years, wire arc additive manufacturing (WAAM) [7–9], a wire-based directed energy deposition (DED) technologies based on an electric arc as the heat source and a solid wire as the feedstock material, see Fig. 1, has increasingly attracted attention in the construction sector. Although the precision of the WAAM technique, the last one was used for fabrication of specimens tested within an on-going project, may be lower than those obtained using powder-bed systems, WAAM are currently accepted in the construction sector both by academia and industry [7–9]. The main reasons for that are: (1) the technique is capable of producing large metallic structural parts in a shorter time due to the increase of deposition rates;

(2) the technique becomes less expensive due to the use of standard off-the-shelf equipment; (3) the techniques become more mature, leading to lower costs due to the decrease of raw material costs.

The current investigations of WAAM steel applications in the construction sector include both modest-scale components and full-size structures [1]. MX3D delivered the first additively manufactured metal pedestrian bridge with a width of 2.5 m and a span of 10 m fabricated by a 6-axis robotic welding arm [10,11]. Bambach et al. [12] exploited the hybrid technologies by combining WAAM and forging, fabricated a rib by depositing layers from a WAAM process on a pre-formed component. The results showed that the hybrid manufactured part shows satisfactory metallurgical bonding in the transition zone. The tensile properties obtained with the samples tested in the transition zone exceed the minimum tensile strength requirements of forged materials. Lange et al. [13,14] redesigned and printed some traditional steel components incorporating the advantages of WAAM and achieved valuable material-savings, such as hook (Fig. 2-a), local stiffener of I-shaped girder, clamping element, optimized T-stub endplate, joints to connect four members (Fig. 2-b) and bridges with a length around 2.5 m. As shown in Fig. 3, ArcelorMittal company, in partnership with Delft

* Corresponding author.

E-mail address: xinhaohui@xjtu.edu.cn (H. Xin).

¹ Present address of the first author.

² Previous address of the first author.

<https://doi.org/10.1016/j.istruc.2021.08.055>

Received 13 November 2020; Received in revised form 21 June 2021; Accepted 17 August 2021

Available online 31 August 2021

2352-0124/© 2021 Institution of Structural Engineers. Published by Elsevier Ltd. All rights reserved.

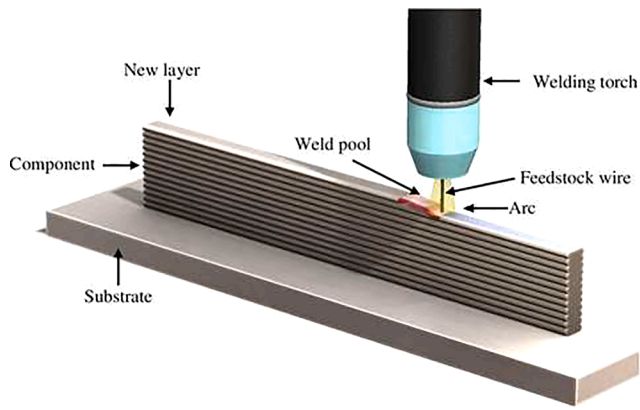


Fig. 1. Schematic of WAAM Process.

University and Technology, developed a new type of pin connections by hybrid manufacturing. The main plate and cover plates were made of S460 steels and the pin connectors were manufactured by GMAW with adequate strength.

Finite element analysis is necessary for understanding and optimizing the performance of AM components [15,16] and especially in the application in connections. Preconditions of FEA is the accurate prediction of the material behavior. Therefore, the coupon specimens were used to evaluate the plastic flow and fracture of WAAM steel plates to

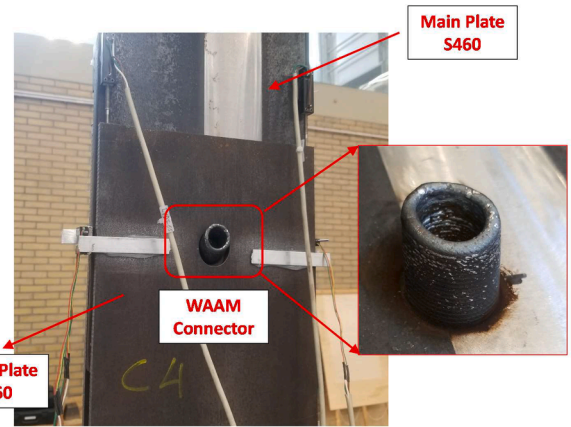
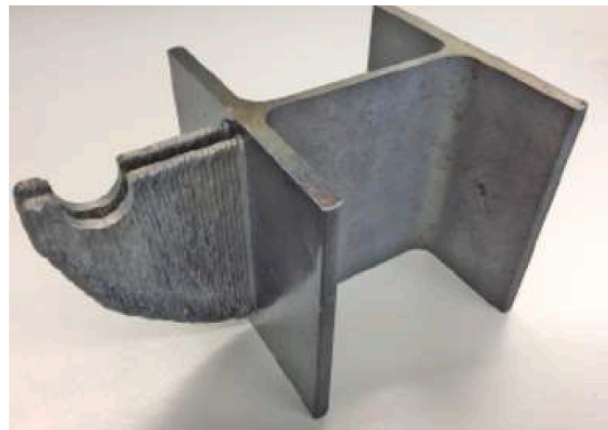
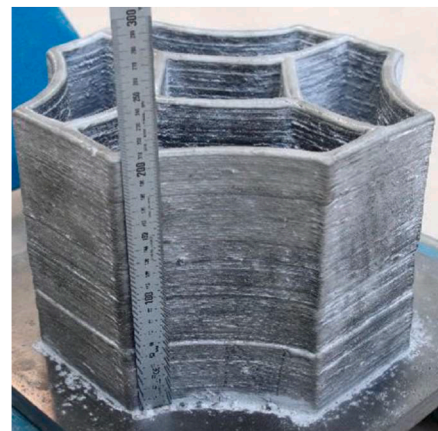


Fig. 3. WAAM Pin Connection manufactured by hybrid manufacturing (Manufactured by ArcelorMittal company and tested in Delft University and Technology).

accomplish an efficient design of structural components. Kyvelou et al. [17] and Laghi [18] conducted a series of tensile tests on WAAM stainless steel on as-built and milled specimens, in an attempt to quantify the material anisotropy by testing coupons cut in different angles to the printing orientation. The results showed that the direction of loading relative to the print layer orientation has a strong influence on the stress–strain characteristics. Coupons loaded by a force 45° to the



(a) Hook [14]



(b) Joints to connect four members [14]

Fig. 2. Photos of conceptual application of WAAM technique in structural connections.

printing direction (“45° coupons”) exhibited the highest values of Young’s modulus and strength while coupons loaded perpendicular to the printing direction (“90° coupons”) had the lowest properties. Szost et al. [19] compared the microstructure and accumulated residual stresses during the fabrication of AM components produced by the WAAM and laser cladding process (CLAD) technique. The results showed that both types of specimens have a very compact material structure with a few pores located in the baseplate vicinity. The maximum residual stresses appeared in the wall-baseplate transition, in both types of specimens, with the higher values if the WAAM technique is used. Wang et al. [20] performed WAAM experiments with 316L stainless steel under different arc modes and a constant deposition rate. The results indicated that the ultimate tensile strengths of the SpeedPulse and SpeedArc additive manufactured specimens along the horizontal direction are greater than 540 MPa, and the tensile strengths and hardness values of the components produced by SpeedArc WAAM are higher than those of components produced by SpeedPulse WAAM due to the finer solidification structure provided by SpeedArc WAAM. Haden et al. [21] investigated the mechanical properties of WAAM steel made of stainless steel 304 and mild steel ER70S respectively. The results showed that no significant difference in yield strength was observed of printed mild steel (ER70S) between specimens cut-out in direction perpendicular and along to the direction of printing, i.e. transversal and longitudinal specimens, while the full stress–strain curves are not compared in terms of different directions. Dinovitzer et al. [22] discussed the process parameters effects on mechanical properties of WAAM steel made of Hastelloy X alloy wire on 304 stainless-steel plate. The results showed that increasing travel speed or decreasing current caused a decrease in melt through the depth and an increase in roughness. Sun et al. [23] experimentally investigated the anisotropic mechanical properties of a low-carbon high-strength steel component fabricated by WAAM. The results showed the mechanical properties of longitudinal specimens were inferior to that of the transversal specimens. Ermakova et al. [24] performed experimental investigation on the mechanical and fracture properties of WAAM components made of ER70S-6 and ER100S-1 metal wires. The results show that the material hardness and yield strength of the specimens fabricated by ER100S-1 were higher than ER70S-6 by 62% and 42%, respectively. The results also showed that the yield and ultimate tensile strength values were slightly higher in “0° specimen” (the printing direction) compared to “90° specimen” (perpendicular to the printing direction). It is evident, based on the recent material investigations, that the level of anisotropy of material fabricated using the WAAM/GMAW technique is important information for material modeling. Still, an open question is whether it is necessary to consider in the design of structural members and connections.

In this paper, the coupon specimens are cut from the plates printed by ArcelorMittal Global R&D Bars & Wires. The specimens are cut in different directions of the printing to quantify material anisotropy.

Three distinct regions of the stress–strain curve obtained in uniaxial coupons are considered in modelling: the elastic stage, the plastic stage and the coupled plastic–damage stage. The FE simulations are performed to derive the true stress and strain curves in different stages.

2. Experimental details

2.1. Description of materials

In detail, the Gas Metal Arch Welding (GMAW), one of WAAM, is used to produce the materials. Four plates, with a dimension of 400 mm × 150 mm × 3.7 mm, were fabricated using welding wire AWS 5.18 ER70S-6 Böhler K56 and getting approximately 1 mm thick layer, see photos of GMAW plates in Fig. 4 and Fig. 5. The chemical composition and mechanical properties of the steel wire are given in Table 1 and Table 2, respectively. The printed plates were milled to 2.8 mm thickness, see Fig. 6, to study the plastic behavior of GMAW plates neglecting the surface roughness effect.

2.2. Specimens preparation

To characterize the anisotropic in-plane plastic behavior of WAAM steel plates at room temperature, material tests along three different orientations have been prepared on smooth dog-bone (SDB) specimens according to specification ASTM E8 [25]. A total of eight specimens were conducted, see Table 3. The geometries of the specimens are presented in Fig. 7 with a nominal width of 6.0 mm and a nominal thickness of 2.8 mm respectively. The actual geometry is also measured by digital caliper during tests and listed in Table 3. The deformation of specimens is recorded by two-dimensional Digital Image Correlation (DIC) while the force is recorded via an electronic universal material testing machine with a capacity of 100.0kN. The gauge length used to calculate engineering strain is defined as 25.0 mm based on ASTM E8 [25]. The tensile tests were conducted in a displacement-controlled mode with a speed of 0.5 mm/min.

2.3. Experimental results

The engineering stress–strain curves of WAAM plates are presented in Fig. 8. The “upper envelope” and “lower envelope” of the results are identified to provide the top and bottom stress bounds at the same strain level of the specimen. The basic material properties, such as the yield strength, ultimate strength, elastic modulus, and uniform elongation are shown in Table 3.

Summary of material characteristic influenced by the printing direction is given below:

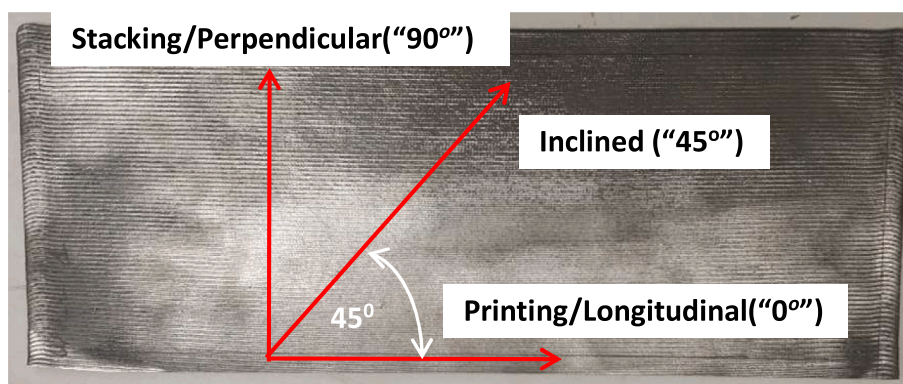


Fig. 4. Naming and orientation of specimens cut from a GMAW plate.



Fig. 5. All four GMAW plates provided for the investigation.

Table 1
Chemical composition of ER70S-6 wire based on EN ISO 636-A standard.

C (%)	Si (%)	Mn (%)	P (%)	S (%)
0.07	1	1.65	0.008	0.0019

- The average elastic modulus along 45° and 90° orientation is 7.71% and 3.80%, respectively, are less compare to the 0° direction, respectively.
- The average yield strength along 45° and 90° orientation is 5.5% and 7.0% larger compare to the 0° direction, respectively.

- The average ultimate strength along 45° and 90° orientation is 1.0% and 2.3% larger compare to the 0° direction, respectively.
- The average uniform elongation along 45° and 90° orientation is 8.0% and 11.7% larger compare to the 0° direction, respectively.

The failure mode of dog-bone specimens is shown in Fig. 9. Obvious necking is observed before the final fracture happens for the specimens in all three different orientations as it would be in the case of mild steel specimens. The obtained fracture plane, which is inclined (slant) in the thickness direction for all specimens, indicating that the shear failure is dominated in the thickness direction. Different from flat fracture mode of the mild steel see Fig. 10, the slant fracture is not only in the appearance of fracture pattern but also the micro-void growth and

Table 2
Mechanical properties of ER70S-6 wire based on EN ISO 636-A standard.

Heat treatment	Yield Strength MPa	Tensile Strength (MPa)	Elongation (L ₀ = 5d ₀) %	Impact energy ISO-V KV J 20 °C	Impact energy ISO-V KV J −40 °C	Wire Diameter mm
As welded	480	580	24	95	47	1.0

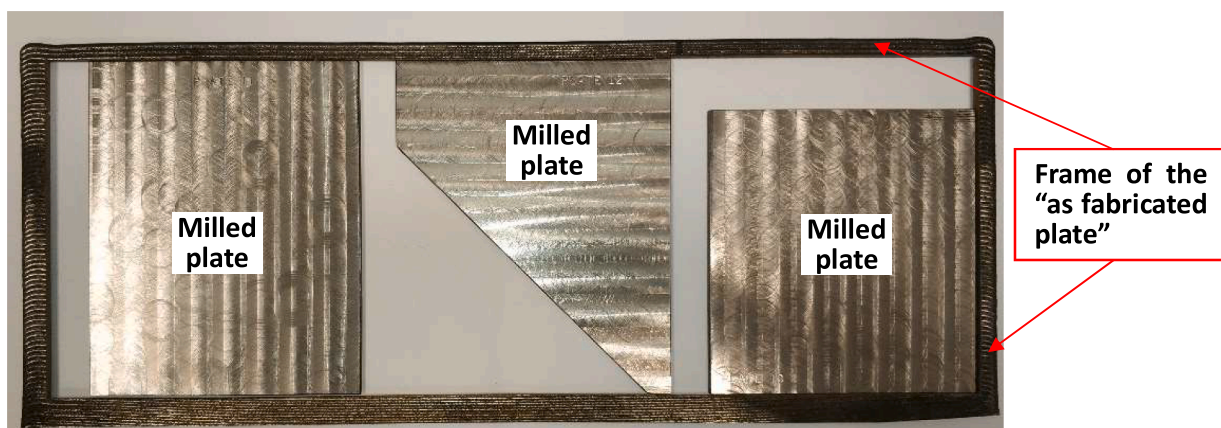


Fig. 6. The milled plate used to cut specimens.

Table 3
Summary of Experimental Results.

Direction	Label	Width (mm)	Thickness (mm)	Elastic Modulus (GPa)	Poisson's ratio	Yield Strength (MPa)	Ultimate Strength (MPa)	Uniform Elongation (%)
0° (L)	L1	6.17	2.82	210.8	0.27	401.6	575.6	27.4
	L2	6.00	2.81	204.2	0.27	382.8	564.0	30.0
	Average			207.5	0.27	392.2	569.8	28.7
45° (I)	I1	5.88	2.82	182.2	0.31	428.9	570.2	32.0
	I2	6.00	2.81	206.9	0.30	418.4	576.8	32.5
	I3	6.00	2.81	185.4	—	393.8	575.4	31.2
	Average			191.5	0.30	413.7	574.1	31.9
90° (T)	P1	6.11	2.87	216.7	0.34	455.7	598.2	31.0
	P2	6.00	2.81	199.4	0.30	408.7	577.3	32.1
	P3	6.05	2.87	182.8	—	394.0	573.6	34.5
	Average			199.6	0.32	419.5	583.0	32.5

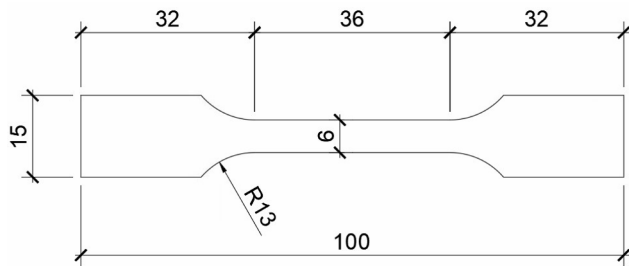


Fig. 7. Geometry of dog-bone specimens (Unit: mm).

coalescence. The shear localization mode, namely large micro-void shape but relatively small volume changes, appeared in the microscale [26] along the thickness direction. The plastic flow in the localized shear bands lead to the ultimate fracture of GMAW plates is observed in all loading orientations.

3. Plastic flow of WAAM plates

3.1. Calibration of plastic flow stress in different printing orientations

The uniaxial stress–strain relationship of GMAW specimens is modelled in three distinct regions: the elastic stage, the plastic stage, and the coupled plastic–damage stage, see Fig. 11. The coupled plastic–damage stage is further decomposed into the plastic-dominated zone and the damage-dominated zone. The elastic stage is controlled by the elastic strain and Young modulus. The plastic and coupled plastic–damage stages are presented in Fig. 11. The relationship of the uniaxial true stress–strain is easily obtained in the plastic stage. Therefore, the main focus point is in modelling of the relationship of uniaxial true stress–strain in the coupled plastic–damage stage. The calibration process is sequential, meaning that the effects of damage-dominated zone is considered separately from the calibration in plastic-dominated zone.

The material is exposed to plastic stage when the equivalent plastic strain is $0 \leq \bar{\epsilon}^p \leq \bar{\epsilon}_u^p$, where $\bar{\epsilon}_u^p$ is the plastic strain when the true stress without considering necking and damage effects reaches the peak, see Fig. 11. In the plastic stage, the uniaxial plastic strain and true stress are simply obtained through the engineering strain - engineering stress relationship, assuming conservation of the volume. The engineering strain ϵ_{en} and engineering stress σ_{en} relationship is simply converted to the true stress σ vs. true strain ϵ relationship using well known equations (2) and (3).

$$\epsilon = \ln(1 + \epsilon_{en}) \tag{2}$$

$$\sigma = \sigma_{en}(1 + \epsilon_{en}) \tag{3}$$

The coupled plastic–damage stage reached when $\bar{\epsilon}_u^p > \bar{\epsilon}^p$. The point of maximum true stress is the onset of the necking. When $\bar{\epsilon}_u^p < \bar{\epsilon}^p \leq \bar{\epsilon}_{d-i}^p$, the

plasticity is dominated in the coupled plastic–damage stage. The weighted function according to Ling [27] shown in Eq.(4), is used to predict the true stress after necking. The measured engineering stress–engineering strain relationship is considered as a target in calibrating the weight constant W , $0 \leq W \leq 1$, using the finite element simulation. The stop criterion of the weight constant W calibration is when one of the following two criterions are satisfied:

The calculated engineering stress is larger than test results when $W = 0$;

The weight constant W in the range $0 \leq W \leq 1$ leads to the calculated engineering stress fitting well the experiment results for strain levels $\bar{\epsilon}_u < \bar{\epsilon} \leq \bar{\epsilon}_{d-i}$, and gives a higher stress prediction when the $\bar{\epsilon} > \bar{\epsilon}_{d-i}$. The point $\bar{\epsilon} = \bar{\epsilon}_{d-i}$ is defined as the onset of the damage-dominated zone of the coupled plastic–damage stage. The corresponding maximum plastic strain, in the finite element model, is defined as the equivalent plastic strain at the onset of damage-dominated zone $\bar{\epsilon}_{d-i}^p$ of the coupled plastic–damage stage.

$$\bar{\sigma}^{neck} = \bar{\sigma}_u \left[W \left(1 + \bar{\epsilon}^p - \bar{\epsilon}_u^p \right) + (1 - W) \left(\frac{\left(\bar{\epsilon}^p \right)^{\bar{\epsilon}_u^p}}{\left(\bar{\epsilon}_u^p \right)^{\bar{\epsilon}_u^p}} \right) \right] \tag{4}$$

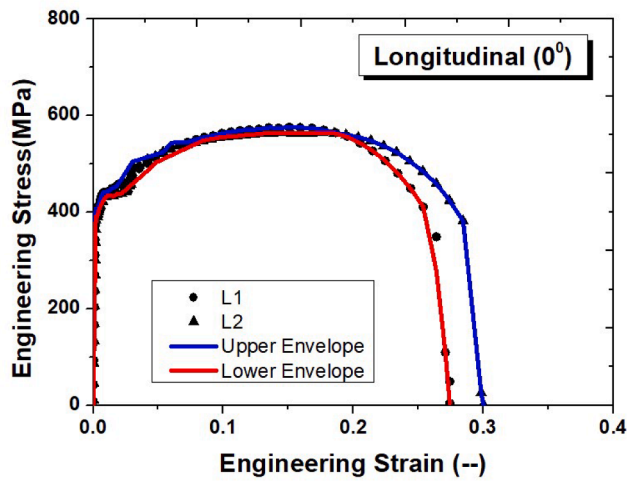
Where: W is a weight constant, $0 \leq W \leq 1$.

The damage is dominated in the coupled plastic–damage stage for strains $\bar{\epsilon}^p > \bar{\epsilon}_{d-i}^p$, see Fig. 11. The true stress in the damage-dominated zone could be obtained through Eq. (5) because the damage effects after necking are not considered in the definition of true stresses. The damage evolution law, expressed in Eq. (6), is assumed in determining the dependence of the damage scalar d on the equivalent plastic strain $\bar{\epsilon}^p$. The experimentally established engineering stress–engineering strain relationship is considered as the objective of the calibration. The parameter B is varied in the finite element model until the calculated engineering curves agree well with the experimental results. The stop criterion of the parameter B calibration is when the difference between the numerical predicted and experimental engineering stress–strain relationship is within 5%. Noted that Eq.(5) and (6) could be iterated several times by adjust the $\bar{\epsilon}_{d-i}^p$ until the predicted engineering stress–strain relationship agreed well with numerical results.

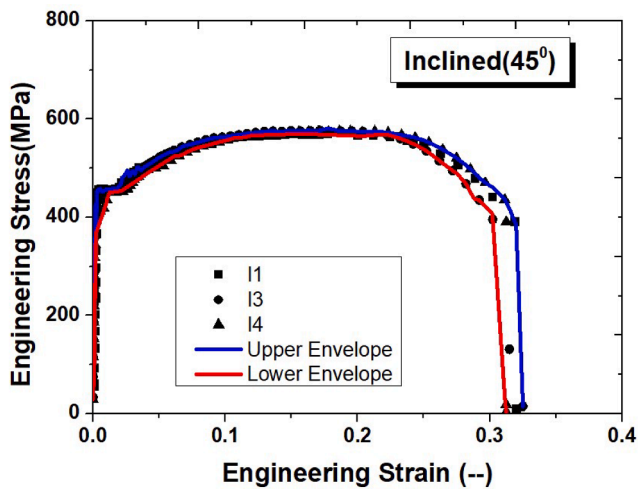
$$\bar{\sigma} = (1 - d) \bar{\sigma}^{neck} \tag{5}$$

$$d = \begin{cases} 0 & \bar{\epsilon}^p < \bar{\epsilon}_{d-i}^p \\ 1 - \exp \left[-B \left(\bar{\epsilon}^p - \bar{\epsilon}_{d-i}^p \right) \right] & \bar{\epsilon}^p \geq \bar{\epsilon}_{d-i}^p \end{cases} \tag{6}$$

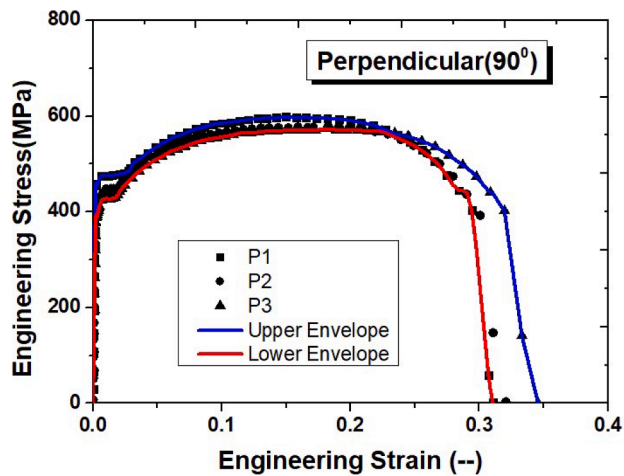
The finite element model and boundary condition used for parameters calibration of coupled plastic–damage stage is shown in Fig. 12. One end of the coupon specimen model is fixed for all displacement at the shown faces, and the other end is used to introduce the displacement. The specimen is modelled by solid element C3D8. The quasi-static simulation is implemented using ABAQUS/EXPLICIT solver with a



(a) Longitudinal

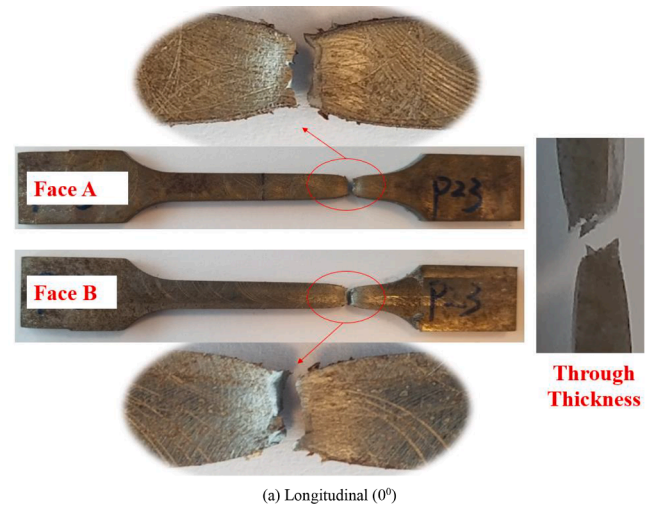


(b) Inclined

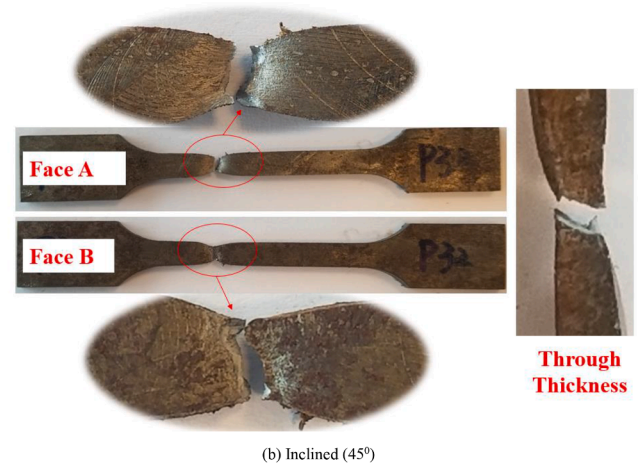


(c) Perpendicular

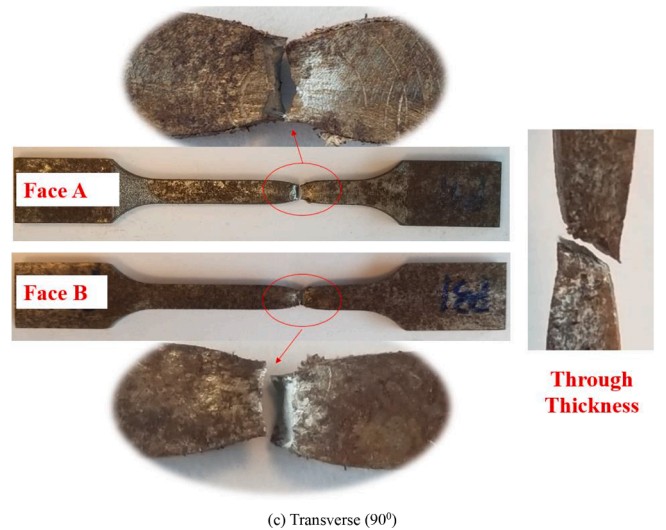
Fig. 8. Engineering stress–strain relationship.



(a) Longitudinal (0°)



(b) Inclined (45°)



(c) Transverse (90°)

Fig. 9. Failure modes of “dog-bone” specimens.

total time 1 s for the mass scaling. Note, no physical meaning of the time step duration.

The time increment influences FE results as shown in Fig. 13. Results of the same model are shown for different time increments using 0.5 mm element in the middle part of the model. The FE results indicate the

predicted results will be affected obviously by the loading rate when the time increment is set as 1×10^{-4} s. Larger variation is observed in the plastic stage and coupled plastic-damage stage. When the time increment is less than 1×10^{-5} s, the minimum increment considered is 1×10^{-7} s, all the models lead to identical engineering stress and strain



(a) t=10mm



(b) t=5mm

Fig. 10. Flat fracture through thickness of cold-formed mild steel S355.

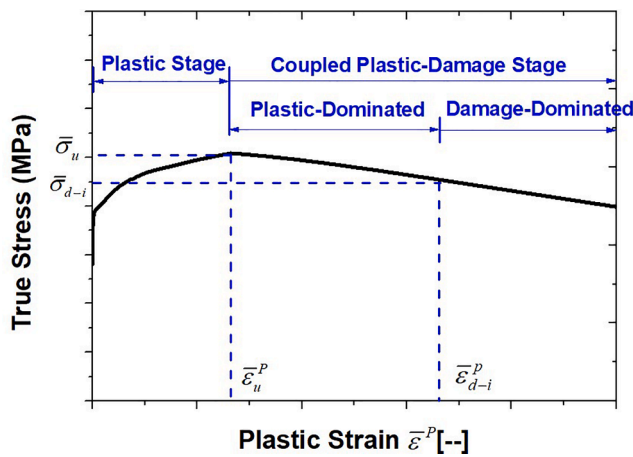


Fig. 11. Plastic and coupled plastic-damage stages (Necking and damage effects are not considered for true stress).

curves, until the force reaches to the peak value. The maximum force represents the onset of the necking. However, the predicted engineering stress of the model in the softening stage, the post necking behavior, using the time increment of 1×10^{-5} s is larger compared to the time increments of 1×10^{-6} s and 1×10^{-7} s. The differences in engineering stress and strain predictions using the time increment 1×10^{-6} s and 1×10^{-7} s are very small. Hence, the time increment 1×10^{-6} s is proposed for the calibration based on 0.5 mm element size in the middle part of the model.

Results of a study of the mesh size effect on FE results are shown in Fig. 14. The investigation is made using FE model, using the time increment 1×10^{-6} s and the same material properties but with different mesh size in the middle part. The coarse mesh will predict the larger engineering stress in the softening stage, see results in Fig. 15. Hence, the mesh size of the flat part of the model for all three orientations is fixed to 0.25 mm to avoid the mesh size effects on the FE results.

The true stress-plastic strain relationship of each stage is calibrated using finite element simulation. The comparisons between FE simulation and experimental results are shown in Fig. 16. A good agreement is

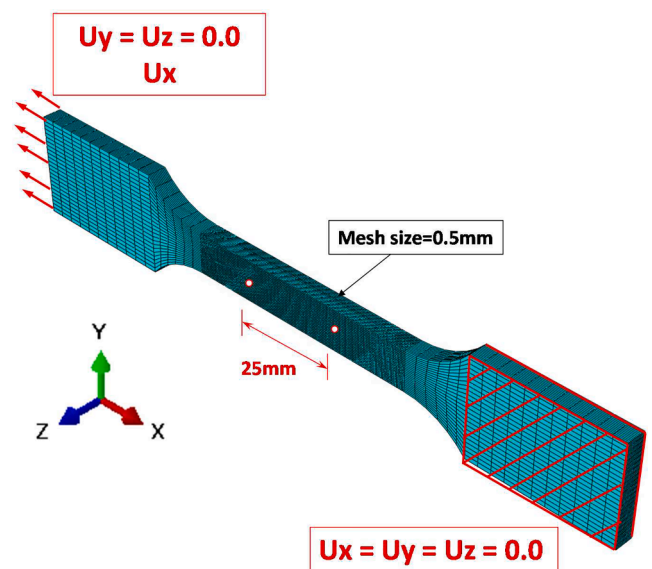


Fig. 12. Finite element model and Boundary conditions.

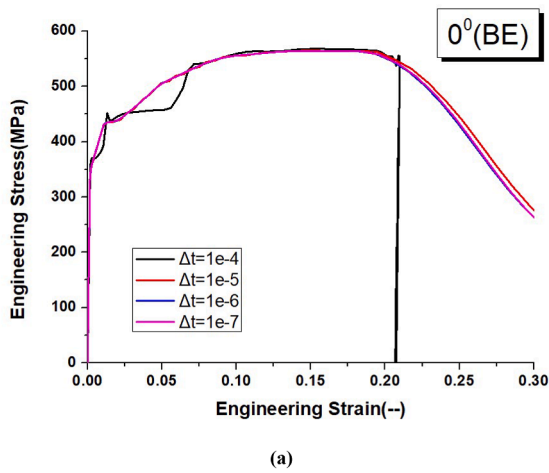
observed. The calibrated parameters for the coupled plastic-damage stage are summarized in Table 4. The calibrated uniaxial stress-strain relationship along three directions are shown in Fig. 17.

Benefits of using true stress-strain shown in Fig. 17 is only in using it in FEA in combination with parameters shown in Table 4. Relatively large difference between upper and lower envelope of true stress-true strain relationship will not have large impact a final prediction of a specimen behavior expresses considering externally applied force and corresponding displacement, as indicated in Fig. 16.

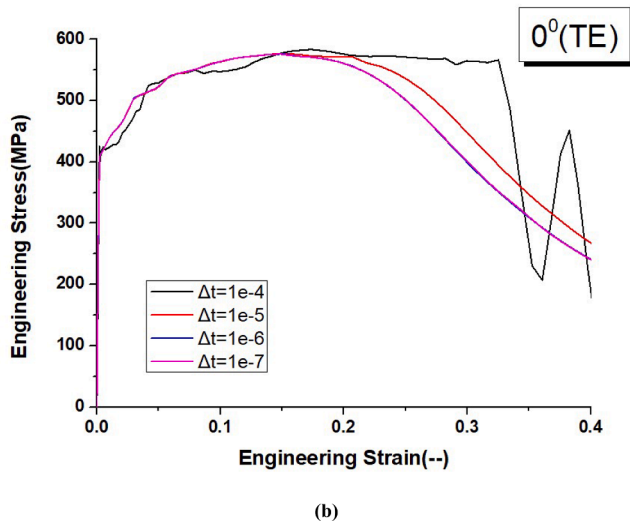
4. Conclusion and future study

4.1. Conclusions

The coupon specimens are cut from the plates printed by

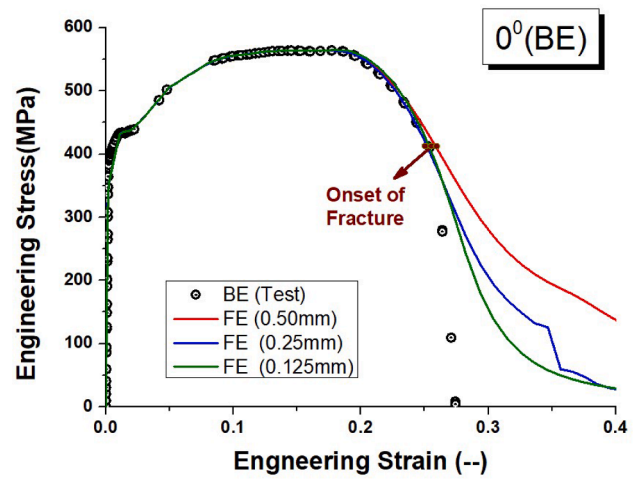


(a)

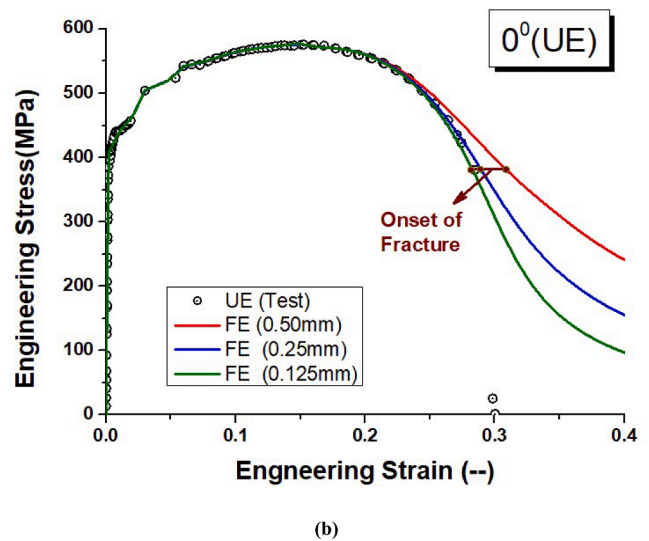


(b)

Fig. 13. The time increment influences FE prediction, the mesh size considered is 0.5 mm.



(a)



(b)

Fig. 15. Mesh size effects on FE simulation results.

stage, the plastic stage and the coupled plastic-damage stage. The FE simulation is performed to obtain the true stress and strain curves in all stages. The following conclusions are drawn:

- (1) The average elastic modulus is 207 GPa, 191 GPa and 200 GPa, and the average yield strength is 392 MPa, 394 MPa and 420 MPa, and the ultimate strength is 570 MPa, 574 MPa, and 583 MPa for GMAW coupon specimens loaded 0° , 45° and 90° to the direction of printing, respectively. The material performance of GMAW steels presented in this paper is comparable to the commercial mild strength steel S460 if the ultimate strength is considered, and S355 if the yield strength value is governing.
- (2) Parameters for material modelling of GMAW are calibrated using uniaxial coupon specimens in the three direction compared to the printing direction. The uniaxial stress-strain relationship consisting of three stages: the elastic stage, the plastic stage, the coupled plastic-damage stage. In order to use the uncoupled fracture model [28] to simulate the ductile fracture of 3D printed material, the true stress-plastic strain relationship of each stage is calibrated through finite element simulation and the sufficiently good agreement is accomplished between FE simulation and experimental results.

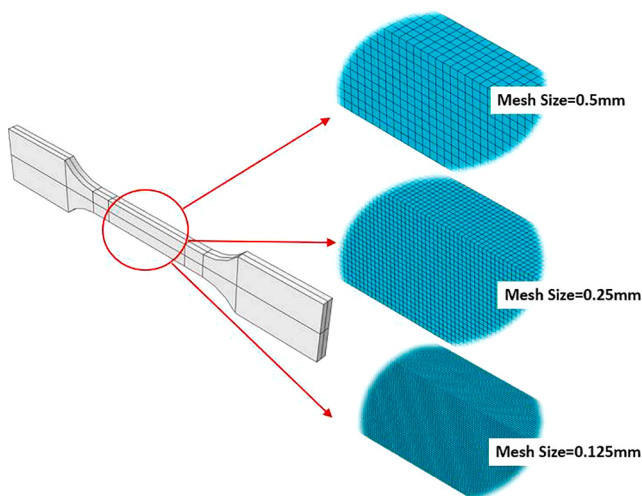


Fig. 14. Different Mesh size of dog-bone specimens.

AccelorMittal Global R&D Bars & Wires. The specimens are cut in different directions related to the printing direction to investigate possible material anisotropy. Results of uniaxial coupon specimens, the stress-strain curve, are considered in three distinct regions: the elastic

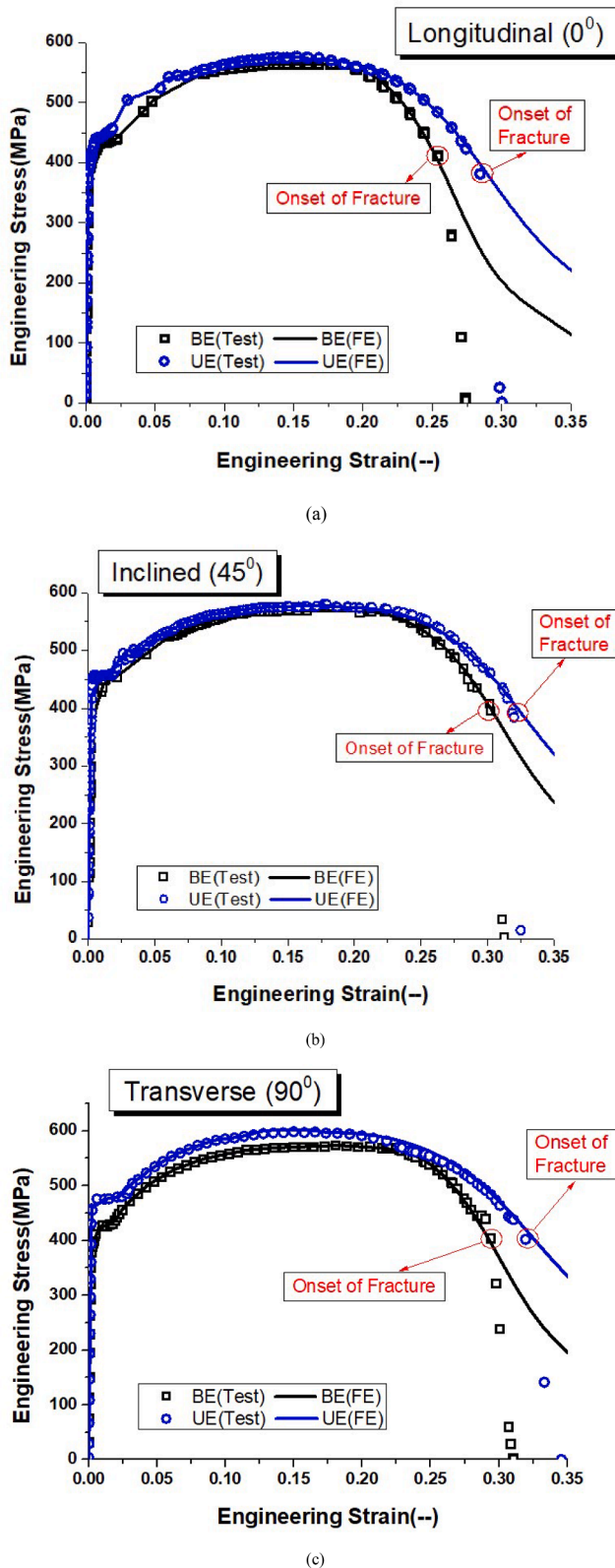


Fig. 16. Comparisons between FE and experimental results.

(3) Anisotropy could be neglected in FEA of GMAW structural components, especially until the onset of necking, based on the calibration of the material parameters. The lower and upper envelope of material parameters could be used to predict a range of the behavior of components as a compensation for the

Table 4
Calibrated parameters for coupled plastic-damage stage.

Description		$\bar{\sigma}_u$ (MPa)	$\bar{\epsilon}_u^p$ (–)	W (–)	$\bar{\epsilon}_{d-i}^p$ (–)	B (–)
0°	BE	667.27	0.1677	0.00	0.1920	0.30
	UE	670.90	0.1600	0.28	–	–
45°	BE	694.07	0.1981	0.00	0.2428	0.05
	UE	700.20	0.1981	0.35	–	–
90°	BE	695.26	0.19921	0.0	0.3892	0.20
	UE	708.92	0.1713	0.60	–	–

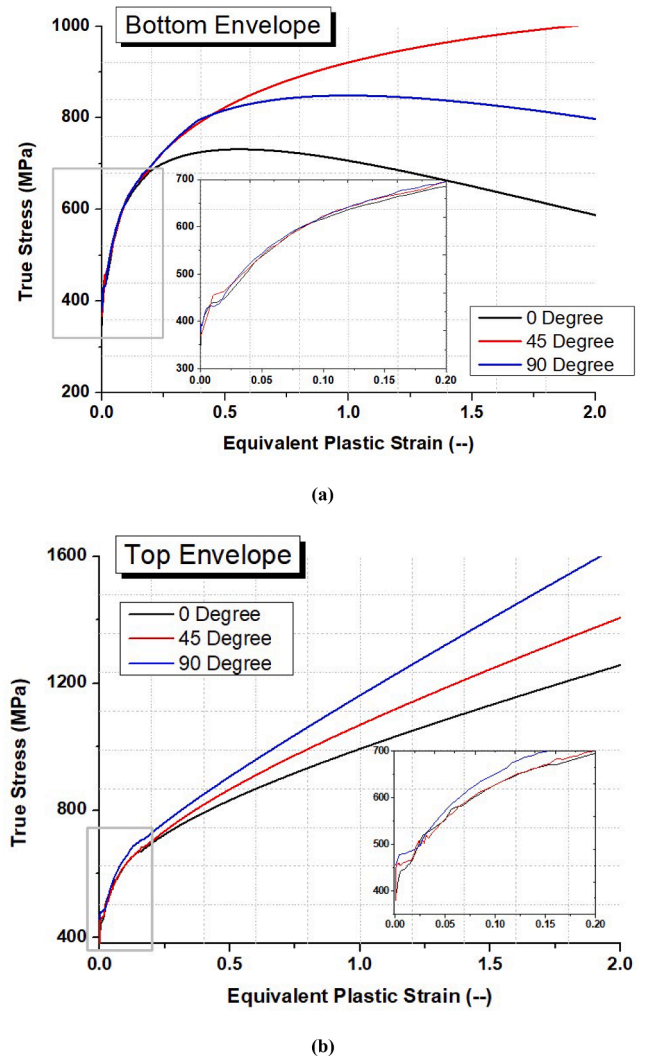


Fig. 17. Uniaxial true stress–strain curves along three orientations.

assumption of isotropic material. The calibrated true stress–plastic strain relationship in this paper is obtained based on the increment time in a quasi-static FEA is 10^{-6} sec, element type of C3D8, and element mesh size 0.25 mm in the critical section.

4.2. Future study

The anisotropic fracture locus of WAAM steel will be further investigated to predict the ductile fracture [29,30] behavior of 3D printed structures.

Declaration of Competing Interest

The authors declare that they have no known competing financial interests or personal relationships that could have appeared to influence the work reported in this paper.

References

- [1] Buchanan C, Gardner L. Metal 3D printing in construction: A review of methods, research, applications, opportunities and challenges. *Eng Struct* 2019;180:332–48.
- [2] Paolini A, Kollmannsberger S, Rank E. Additive manufacturing in construction: A review on processes, applications, and digital planning methods. *Addit Manuf* 2019;30:100894. <https://doi.org/10.1016/j.addma.2019.100894>.
- [3] Jovasevic S, Correia J, Pavlovic M, Dantas R, Rebelo C, Veljkovic M, et al. Alternative steel lattice structures for wind energy converters. *Int J Struct Integr* 2019.
- [4] Wang Z, Wu W, Qian G, Sun L, Li X, Correia J. In-situ SEM investigation on fatigue behaviors of additive manufactured Al-Si10-Mg alloy at elevated temperature. *Eng Fract Mech* 2019;214:149–63.
- [5] Fiorentin F, Oliveira B, Pereira J, Correia J, de Jesus AMP, Berto F. Fatigue Behavior of Metallic Components Obtained by Topology Optimization for Additive Manufacturing. *Frat Ed Integrità Strutt* 2021;15:119–35.
- [6] Standard A. ISO/ASTM 52900: 2015 Additive manufacturing-General principles-terminology. ASTM F2792-10e1 2012.
- [7] Rodrigues TA, Duarte V, Miranda RM, Santos TG, Oliveira JP. Current status and perspectives on wire and arc additive manufacturing (WAAM). *Materials (Basel)* 2019;12(7):1121. <https://doi.org/10.3390/ma12071121>.
- [8] Cunningham CR, Flynn JM, Shokrani A, Dhokia V, Newman ST. Invited review article: strategies and processes for high quality wire arc additive manufacturing. *Addit Manuf* 2018;22:672–86.
- [9] Wu B, Pan Z, Ding D, Cuiuri D, Li H, Xu J, et al. A review of the wire arc additive manufacturing of metals: properties, defects and quality improvement. *J Manuf Process* 2018;35:127–39.
- [10] Anderson GS. 3D printed steel pedestrian bridge will soon span an Amsterdam canal. *3D Print* 2015.
- [11] Gardner L, Kyvelou P, Herbert G, Buchanan C. Testing and initial verification of the world's first metal 3D printed bridge. *J Constr Steel Res* 2020;172:106233. <https://doi.org/10.1016/j.jcsr.2020.106233>.
- [12] Bambach M, Sizova I, Sydow B, Hemes S, Meiners F. Hybrid Manufacturing of Components from Ti-6Al-4 V by Metal Forming and Wire-Arc Additive Manufacturing. *J Mater Process Technol* 2020;282:116689. <https://doi.org/10.1016/j.jmatprotec.2020.116689>.
- [13] Feucht T, Lange J, Waldschmitt B, Schudlich A-K, Klein M, Oechsner M. Welding Process for the Additive Manufacturing of Cantilevered Components with the WAAM. *Adv. Join. Process.: Springer*; 2020. p. 67–78.
- [14] Lange Jörg, Feucht T, Erven M. 3D printing with steel: Additive Manufacturing for connections and structures. *Steel Constr* 2020;13(3):144–53.
- [15] Xin H, Sun W, Fish J. A surrogate modeling approach for additive-manufactured materials. *Int J Multiscale Comput Eng* 2017;15(6):525–43. <https://doi.org/10.1615/IntJMCompEng.v15.i6.101615/IntJMCompEng.2017024632>.
- [16] Xin H, Sun W, Fish J. Discrete element simulations of powder-bed sintering-based additive manufacturing. *Int J Mech Sci* 2018;149:373–92.
- [17] Kyvelou P, Slack H, Mountanou DD, Wade MA, Britton T Ben, Buchanan C, et al. Mechanical and microstructural testing of wire and arc additively manufactured sheet material. *Mater Des* 2020:108675.
- [18] Vittoria Laghi, Michele Palermo, Giada Gasparini, Milan Veljkovic TT. Assessment of design mechanical parameters and partial safety factors for Wire-and-Arc Additive Manufactured stainless steel. *Eng Struct* 2020;225:11314.
- [19] Szost BA, Terzi S, Martina F, Boisselier D, Prytuliak A, Pirling T, et al. A comparative study of additive manufacturing techniques: Residual stress and microstructural analysis of CLAD and WAAM printed Ti-6Al-4V components. *Mater Des* 2016;89:559–67.
- [20] Wang L, Xue J, Wang Q. Correlation between arc mode, microstructure, and mechanical properties during wire arc additive manufacturing of 316L stainless steel. *Mater Sci Eng A* 2019;751:183–90.
- [21] Haden CV, Zeng G, Carter FM, Ruhl C, Krick BA, Harlow DG. Wire and arc additive manufactured steel: Tensile and wear properties. *Addit Manuf* 2017;16:115–23.
- [22] Dinovitzer M, Chen X, Laliberte J, Huang X, Frei H. Effect of wire and arc additive manufacturing (WAAM) process parameters on bead geometry and microstructure. *Addit Manuf* 2019;26:138–46.
- [23] Sun L, Jiang F, Huang R, Yuan D, Guo C, Wang J. Anisotropic mechanical properties and deformation behavior of low-carbon high-strength steel component fabricated by wire and arc additive manufacturing. *Mater Sci Eng A* 2020:139514.
- [24] Ermakova A, Mehmanparast A, Ganguly S, Razavi J, Berto F. Investigation of mechanical and fracture properties of wire and arc additively manufactured low carbon steel components. *Theor Appl Fract Mech* 2020;109:102685. <https://doi.org/10.1016/j.tafmec.2020.102685>.
- [25] Astm E. Standard test methods for tension testing of metallic materials. *Annu B ASTM Stand ASTM* 2001.
- [26] Weck A, Wilkinson DS. Experimental investigation of void coalescence in metallic sheets containing laser drilled holes. *Acta Mater* 2008;56(8):1774–84.
- [27] Ling Y. Uniaxial true stress-strain after necking. *AMP J Technol* 1996;5:37–48.
- [28] Xin H, Veljkovic M. Evaluation of High Strength Steels Fracture Based on Uniaxial Stress-Strain Curves. *Eng Fail Anal* 2021;120:105025.
- [29] Xin H, Veljkovic M, José AFO, Correia FB. Ductile fracture locus identification using mesoscale critical equivalent plastic strain. *Fatigue Fract Eng Mater Struct* 2021:1–13.
- [30] Xin H, Correia J, Veljkovic M, Berto F. Fracture parameters calibration and validation for the high strength steel based on the mesoscale failure index. *Theor Appl Fract Mech* 2021;112:102929. <https://doi.org/10.1016/j.tafmec.2021.102929>.